Journal of Nuclear Materials 514 (2019) 255–265

Contents lists available at ScienceDirect

Journal of Nuclear Materials

journal homepage: www.elsevier.com/locate/jnucmat

Ion irradiation effects on commercial PH 13-8 Mo maraging steel Corrax

Ce Zheng [a], Ryan Schoell [a], Peter Hosemann [b], Djamel Kaoumi [a, *]

[a] Department of Nuclear Engineering, North Carolina State University, Raleigh, NC, 27695-7909, USA
[b] Department of Nuclear Engineering, University of California, Berkeley, CA, 94720-1730, USA

GRAPHICAL ABSTRACT

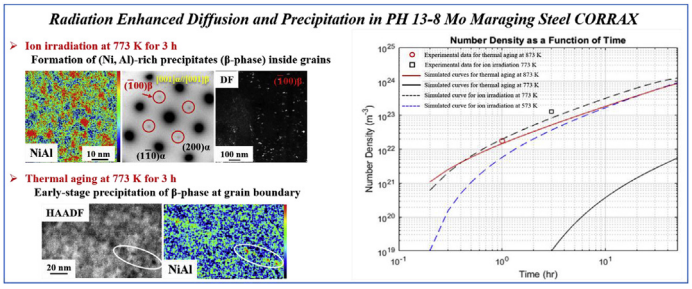

ARTICLE INFO

Article history:
Received 18 September 2018
Received in revised form
29 November 2018
Accepted 30 November 2018
Available online 1 December 2018

Keywords:
PH 13-8 Mo maraging steel
Corrax
ChemiSTEM
In-situ ion irradiation
Radiation-induced precipitation
Radiation-enhanced diffusion
Precipitate nucleation

ABSTRACT

The effects of irradiation on the precipitation behavior of commercial PH 13-8 Mo maraging steel a.k.a. Corrax are investigated through in-situ ion irradiation. Samples of the alloy in its solution annealed state are irradiated up to 10 dpa at 573 and 773 K using 1 MeV Kr ions, in-situ in a transmission electron microscope in order to probe irradiation effects on the precipitation usually observed in this alloy under thermal aging. Indeed, the alloy is known to develop a relatively fine distribution of precipitates during thermal aging which gives the martensitic alloy its strength. The effects of irradiation are substantiated by comparing with the same material thermally aged at 773 and 873 K for similar amounts of experimental time. Both radiation and thermal aging induced segregation and precipitation are characterized using analytical transmission electron microscopy (TEM) techniques.

The diffusion coefficients under irradiation are estimated using the point defect balance equations based on Rate Theory and then compared with the thermal diffusion coefficients, demonstrating the accelerated precipitation of β-phase and Laves-phase in the irradiation case at relatively lower temperature is attributed to the radiation-enhanced diffusion. In addition, a numerical model based on classical precipitate nucleation and growth theories is introduced and shows a relatively good agreement with the experimental results in terms of precipitate density. This study serves to generate baseline data on ion irradiation effects on Corrax to learn how this steel responds to irradiation.

1. Introduction

Maraging steels are low-carbon, high strength steels which are suited for a variety of different applications including aircraft and

* Corresponding author. Department of Nuclear Engineering, North Carolina State University, 2500 Stinson Dr, #2115, Raleigh, NC, 27695, USA.
E-mail address: dkaoumi@ncsu.edu (D. Kaoumi).

https://doi.org/10.1016/j.jnucmat.2018.11.041
0022-3115/

aerospace industries (e.g. landing gear, helicopter undercarriages and rocket motor cases) as well as medical and dental equipments [1–3]. The high strength of this type of steels results from the formation of nano-sized intermetallic compounds under thermal aging [4–7]. Depending on the alloying elements added to maraging steels, different intermetallic compounds can form. The formation of hexagonal η-phase ($Ni_3(Ti,Al)$) precipitates in Ti-containing maraging steels has been reported in literature [8–11]. Another type of precipitate phase, "G-phase" ($Ti_6Si_7Ni_{16}$), was found in Ti-containing maraging steels when additionally alloyed with Si [6,11,12]. The shape of the η-phase is thought to be rod-like, while the G-phase shows a spherical morphology. Furthermore, the spatial distributions of η-phase and G-phase in thermal aged maraging steels is usually non-uniform [13,14]. Later studies by Simm et al. [15] et Gray et al. [16] showed large size precipitates, namely Laves-phase, also existed in (Co, W)-containing maraging steels. The Laves-phase has a lower number density and a more irregular shape compared with η-phase and G-phase.

In contrast, the ordered β-phase (Ni,Al), which is formed in PH 13-8 Mo steels containing Ni and Al, exhibits a uniform distribution within the matrix [6,7,11,17,18]. The β-phase is known to have a B2 (CsCl) super-lattice structure consisting of two interpenetrating primitive cubic cells, where the Al atoms occupy the cube corners of the first sub-lattice and the Ni atoms occupy the cube corners of the second sub-lattice. The lattice constant of the stoichiometric phase is 0.289 nm [19], which is quite close to the lattice constant of the Fe-Cr matrix (~0.287 nm [20]). Due to this fact, the β-phase is coherent with the matrix and has the smallest lattice mismatch compared with η-phase and G-phase. Such coherent precipitates with a relatively fine distribution could act as efficient defect sinks for point defects induced by irradiation. Hence, PH 13-8 Mo maraging steels could be a potential candidate material for nuclear applications. Unfortunately, the irradiation response of such maraging steels is not very well known. Some recent studies reported irradiation effects on mechanical properties of PH 13-8 Mo maraging steels [21–25], however, very few studies focused on irradiation effects on the alloy microstructure itself. Van Renterghem et al. [24] studied the stability of β-phase precipitates in thermally aged PH 13-8 Mo maraging steel irradiated with neutrons to 2 dpa at 573 K. Post-irradiation characterization showed that the β-phase was still present, and the precipitate size did not grow or shrink due to neutron irradiation. Hofer et al. [25] compared the size and number density of β-phase precipitates in PH 13-8 Mo maraging steel before/after proton irradiation to 2 dpa at 273 K. The material was aged at 773 K for 2 h before irradiation. Therefore, it is not a surprise that the β-phase was already observed before irradiation by Atom Probe Tomography (APT). The post-irradiation APT analysis revealed that the size and number density of the β-phase were not influenced by proton irradiation. Besides, Hofer et al. [25] also investigated the effects of proton irradiation at room temperature on the solution annealed PH 13-8 Mo maraging steel. After 2 dpa proton irradiation at room temperature, the β-phase was not observed directly from the 3D reconstructed elemental maps. However, the frequency distribution analysis detected signs of decomposition mainly enriched in Ni and Si. Using Rate Theory to calculate the diffusion coefficients under irradiation, the authors assumed that the diffusion induced by irradiation was just high enough to allow decomposition but still too low for a full precipitation.

So far, for solution annealed PH 13-8 Mo maraging steel, the effects of irradiation on the microstructure were only investigated at low doses at room temperature. In this study, we look at the behavior of solution annealed PH 13-8 Mo steel under ion irradiation to high doses at elevated temperatures. The precipitate nucleation process and growth kinetics in ion irradiated samples are followed in-situ in a transmission electron microscope and compared with similar samples thermally aged also in the microscope for equivalent amounts of time. The resulting precipitate population is compared for the two cases and using analytical transmission electron microscopy (TEM) techniques. Point defect balance equations from Rate Theory are used to estimate the diffusion coefficients under irradiation and a numerical model based on classical precipitation nucleation and growth theories is introduced and compared with the experimental results, in terms of precipitate density as a function of time. This study serves to generate baseline data on ion irradiation effects on Corrax to learn how this steel responds to irradiation.

2. Experimental

The commercial PH13-8Mo maraging steel Corrax (heat No. U74620) was obtained from Bohler-Uddeholm Corp. Its nominal compositions in wt% and at% are given in Table 1. The alloy was solution-heat-treated at 1123 K for 0.5 h and subsequently air cooled to room temperature, resulting in a hardness of 34 HRC and a yield strength of 700 MPa [26]. The alloy was received in its solution-annealed state. TEM specimens were prepared using a FEI Quanta 3D Focused Ion Beam (FIB) instrument. The FIB lift-out technique used was described in details elsewhere [27]. At the end of sample preparation, a low energy 2–5 keV Ga^+ ion beam was used to remove TEM-visible FIB surface damage.

In-situ experiments were carried out at the Intermediate Voltage Electron Microscope (IVEM) Facility at Argonne National Laboratory. The facility consists of a Hitachi 9000 NAR transmission electron microscope coupled with a 500 keV NEC implanter. TEM specimens were irradiated in the microscope using 1 MeV Kr^{2+} ions with an incident angle of 30° from the electron beam and typically ~13-16° from the specimen normal. During irradiation, the flux was kept at 6.25×10^{15} ions·m^{-2}·s^{-1} and measured to an accuracy of ±10% using an annular Faraday cup. The irradiation dose rate in displacement per atom per second (dpa·s^{-1}) was estimated using the software package SRIM-2008 [28] under the "Kinchin-Pease calculation" mode (a.k.a. "quick damage calculation" mode). The default density of 7.86×10^3 kg m^{-3} and displacement energies of 40 eV for metallic elements and 28 eV for other nonmetallic elements were used [29]. The blue curve in Fig. 1 represents the damage profile of 1 MeV Kr^{2+} ions obtained with SRIM. The damage profile is relatively uniform through the first 100 nm of the total range of 500 nm, resulting in an irradiation dose rate of ~1.07×10^{-3} dpa·s^{-1} in the first 100 nm depth (corresponding to the thickness of TEM specimens). Overall, two TEM specimens were subject to total fluences of 5.86×10^{19} ions·m^{-2} (~10 dpa) at 573 K and 2.93×10^{19} ions·m^{-2} (~5 dpa) at 773 K, respectively. In order to investigate thermal effects alone, two other TEM specimens were held at 773 and 873 K in the microscope for 3 and 1 h, respectively. The experimental time for aging at 773 K is consistent with the total time spent during the irradiation experiment at the same temperature. Irradiation and thermal aging temperatures were measured by a thermocouple attached to the heating cup of the holder and was kept within ±5 K of the nominal temperature.

Ion irradiated and thermally aged Corrax specimens were then characterized using a FEI Titan 80–300 probe aberration corrected

Table 1
Nominal chemical compositions (wt% and at%) of Corrax (heat No. U74620).

Element	Fe	Cr	Ni	Al	Mo	Mn	Si	C
wt%	Bal.	11.9	9.11	1.78	1.36	0.29	0.24	0.029
at%	Bal.	12.52	8.49	3.61	0.78	0.29	0.47	0.13

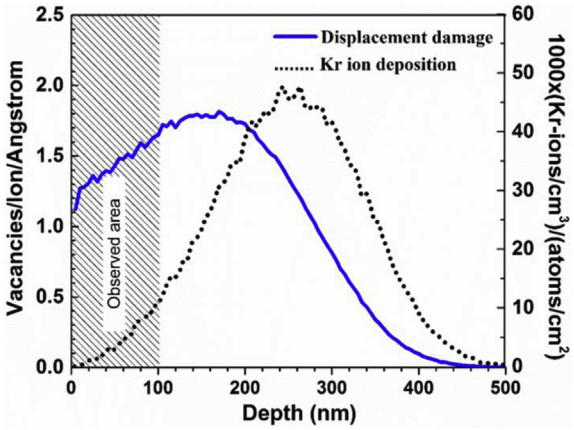

Fig. 1. SRIM calculations showing the damage profile and retention of Kr ions vs. depth in Corrax irradiated with 1 MeV Kr^{2+} ions.

scanning/transmission electron microscope. Precipitation and chemical segregation were examined using the "ChemiSTEM" method. Previous studies [30,31] have shown that this method is very efficient for characterizing radiation-induced precipitation and segregation in ion irradiated Fe-Cr alloys. Precipitates and dislocations (including radiation-induced dislocation loops) were also imaged using conventional TEM techniques such as selection area electron diffraction (SAED), bright field (BF) and dark field (DF) imaging methods. The specimen thickness was measured using the electron energy loss spectroscopy (EELS) zero loss method [32]. Hand-counting techniques and the image processing software ImageJ were used to measure the size and number density of precipitates and dislocations from elemental maps and TEM-BF images.

3. Results

3.1. As-received state

As shown in Fig. 2(a), the microstructure of the as-received Corrax mainly consists of martensitic lath grains, which is in good agreement with previous XRD measurements reported in Refs. [33,34]. Neither segregation of alloying elements to grain boundaries nor precipitation are noticed in the as-received Corrax, as evidenced in the ChemiSTEM elemental maps of Fig. 2(b).

3.2. Thermal aging at 773 and 873 K

Fig. 3(a) shows the depletion of Cr and Mn and the enrichment of Al, Mo, Ni and P at/near the same grain boundary in the sample thermally aged at 773 K for 3 h. The observations indicate the high mobility of alloying elements results from thermal diffusion. Moreover, the Cr concentration profile across the grain boundary exhibits a "W" shape, indicating the depletion of Cr is not at the grain boundary but rather at the troughs of the "W". In literature, a similar "W"-shaped Cr depletion profile caused by radiation induced segregation was observed in austenitic steels under neutron and proton irradiation [35,36]. Cole et al. [36] attributed the formation of the "W"-shaped profile to the binding of the Cr atoms with impurity atoms such as P at the grain boundary. While the Cr at the boundary is held by the impurity atoms, Cr adjacent to the boundary can freely diffuse, thus resulting in near boundary depletion and consequently the "W" profile. Similar mechanism can be invoked in our thermally aged sample with the diffusion being thermal in nature.

In addition to the chemical segregation/depletion profile, early-stage precipitation is also observed in the same sample aged at 773 K. As shown in Fig. 3(b), the (Ni, Al)-rich precipitates with diameter of 2–4 nm nucleate along the grain boundary where Ni and Al also segregate. However, no precipitation is observed inside the martensitic laths. In contrast, intra-granular precipitation (i.e. inside the martensitic laths) is clearly observed in Corrax thermally aged at 873 K for 1 h. Fig. 4(a) shows the precipitates are enriched in Ni and Al, and exhibits a uniform distribution within the matrix. These (Ni,Al)-rich precipitates are also known as the β-phase. The SAED analysis shown in Fig. 4(b) reveals the presence of super-lattice reflections in addition to the matrix reflections near the [100] zone axis in Corrax aged at 873 K. The super-lattice reflections corresponding to the β-phase are identified as a B2 (CsCl) super-lattice structure consisting of two interpenetrating primitive cubic cells, where the Al atoms occupy the cube corners of the first sublattice and the Ni atoms occupy the cube corners of the second sublattice [17,18]. The lattice constant of the super-lattice is measured as ~0.281 nm, which is quite close to the nominal lattice constants of β-phase (~0.289 nm [19]) and the matrix of Fe-Cr (~0.287 nm [20]). The β-phase precipitates are also observed in the TEM-DF micrograph imaged with the $(\bar{1}00)$ super-lattice reflection, as evidenced in Fig. 4(b).

Apart from the β-phase, another type of precipitates (Laves-phase) is also observed in Corrax thermally aged at 873 K. Fig. 5(a)

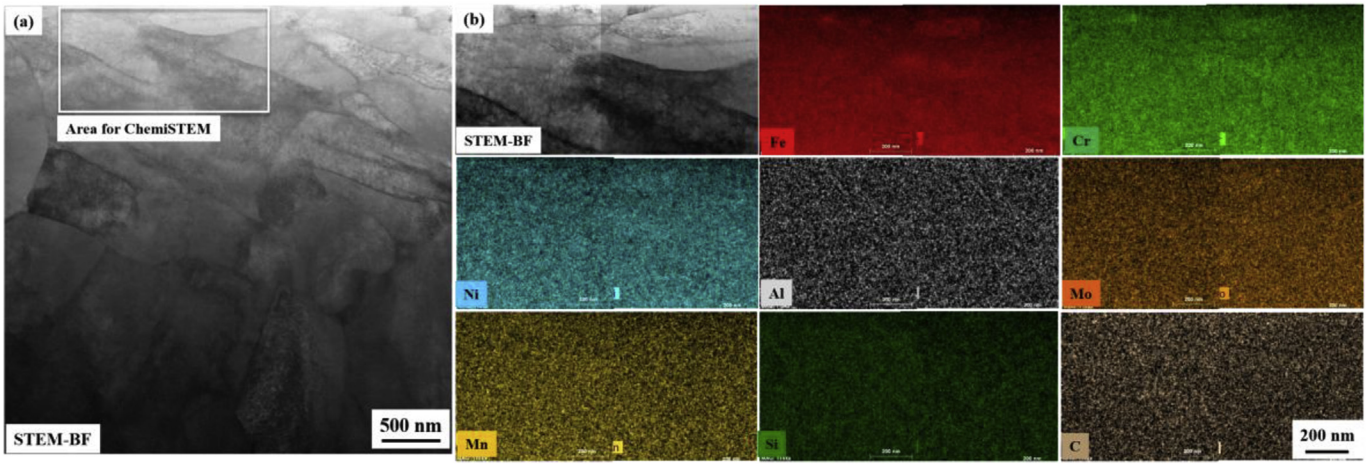

Fig. 2. (a) The STEM-BF micrograph of the as-received Corrax; (b) ChemiSTEM maps revealing neither segregation of alloying elements to grain boundaries nor precipitation of any new phases are observed in the as-received Corrax.

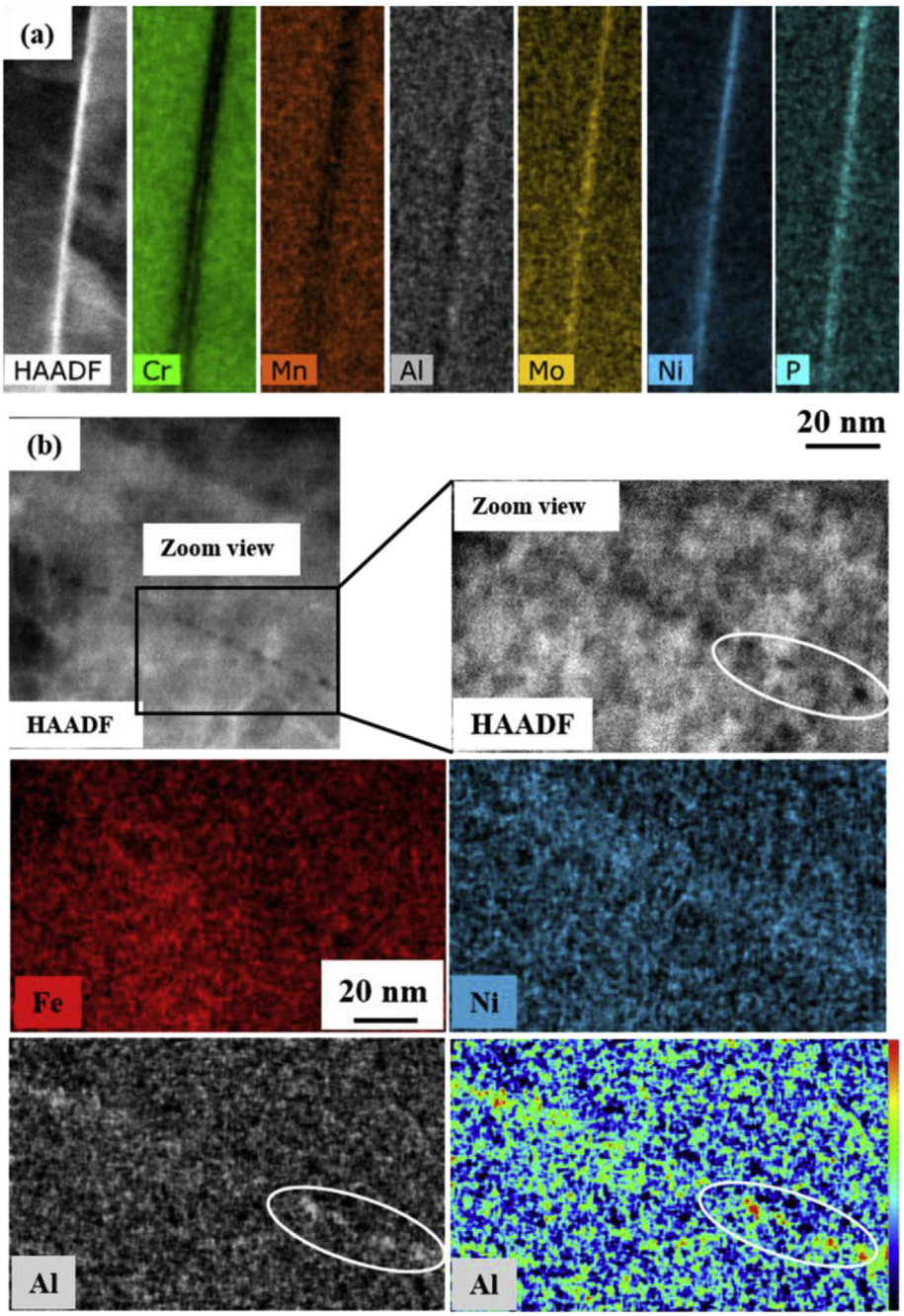

Fig. 3. Corrax thermally aged at 773 K: ChemiSTEM maps showing (a) the depletion of Cr, Mn and segregation of Al, Mo, Ni and P to the same grain boundary; (b) the Al-rich precipitates nucleate along with the grain boundary to which Ni and Al also segregate.

shows the Laves-phase precipitates are depleted in Fe and enriched in Cr, Mn and Mo. These precipitates are further observed in the TEM-BF and -DF micrographs, as evidenced in Fig. 5(b). In contrast with the β-phase, the Laves-phase exists both in spherical and elongated elliptical shapes. To the best of the authors' knowledge, the Laves-phase precipitation in PH 13-8 Mo maraging steel (Corrax) under thermal aging has never been reported in literature. However, the formation of Laves-phase were observed in other (Co, W)-containing maraging steels under thermal aging. Simm et al. [15] studied a low-Al maraging steel by Atom Probe Tomography (APT) and observed a Mo-rich Laves-phase after austenitization and aging at 813 K for 7.5 h. A Laves phase was also observed using the same characterization method by Gray et al. [16] in a novel maraging steel F1E austenitized at 1098–1233 K for 1 h. Moreover, after thermal aging the same material at 793–833 K for times between 1 and 24 h, the same authors reported the formation of a new Laves phase. Both Laves-phases were identified as (Mo, W)-rich precipitates with an irregular elliptical shape and the authors suggested that the nature of the Laves-phase precipitates strongly depended on chemical compositions of maraging steels and temperatures of the austenitization and aging processes.

3.3. Ion irradiation at 573 and 773 K

ChemiSTEM maps of Corrax irradiated to 10 dpa at 573 K are shown in Fig. 6. Radiation-induced segregation of Ni at the grain

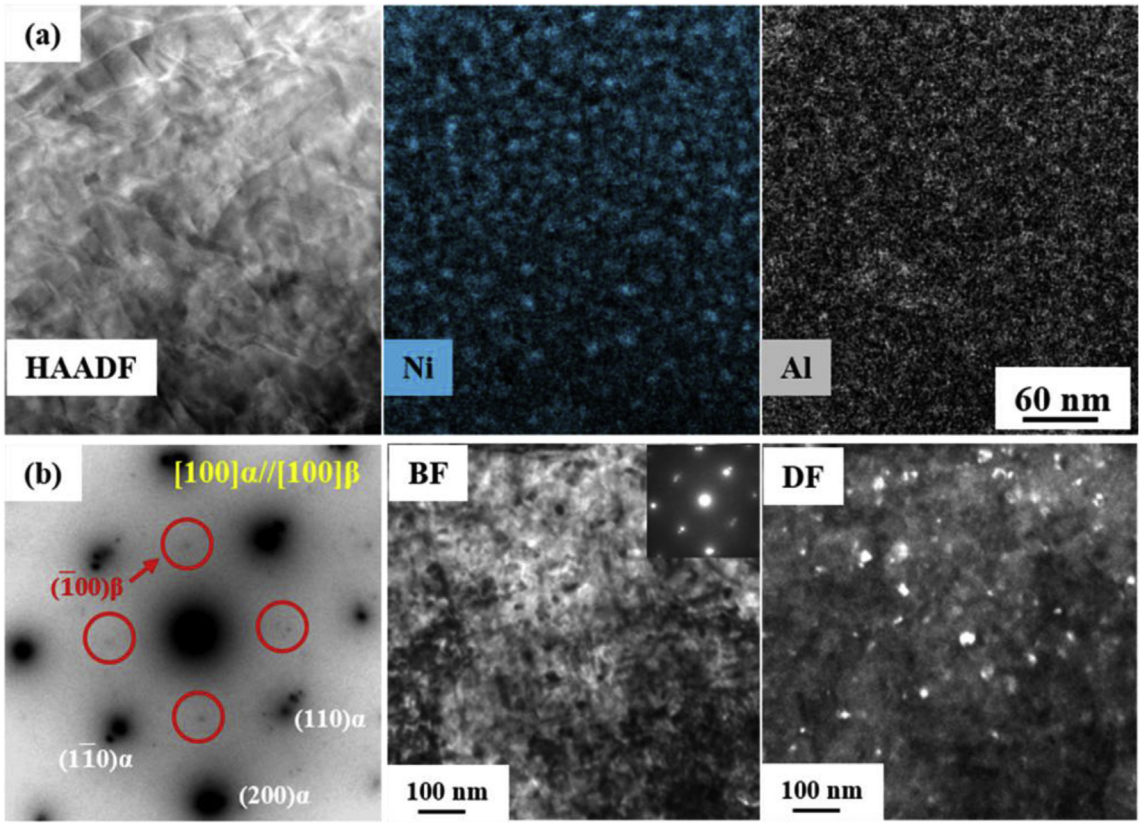

Fig. 4. Corrax thermally aged at 873 K: (a) ChemiSTEM maps showing the formation of (Ni,Al)-rich precipitates (a.k.a β-phase); (b) The SAED analysis showing the super-lattice reflections of β-phase and reflections of the martensitic matrix near the [100] zone axis. The precipitates are observed in the TEM-DF micrograph imaged with the ($\bar{1}$00) super-lattice reflection.

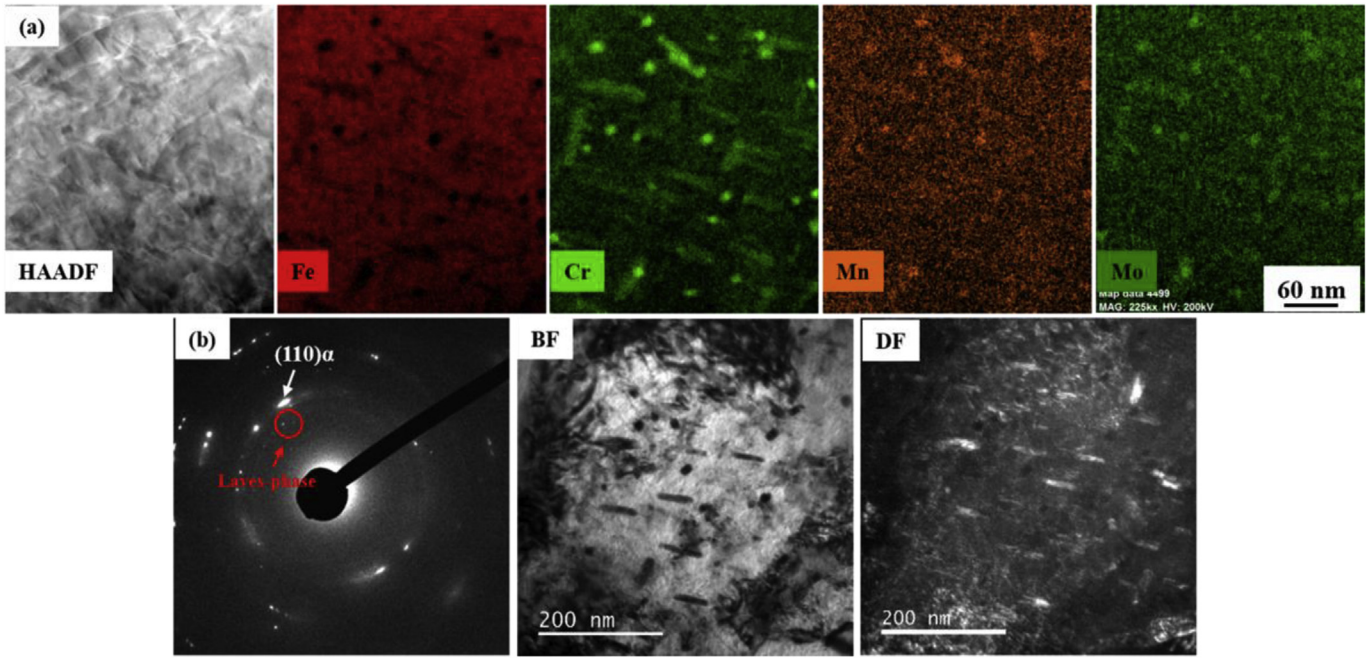

Fig. 5. Corrax thermally aged at 873 K: (a) ChemiSTEM maps showing the formation of (Cr,Mn,Mo)-rich precipitates (a.k.a Laves-phase); (b) TEM-BF and corresponding TEM-DF micrographs showing the formation of Laves-phase precipitates.

boundary is observed, however, neither β-phase nor Laves-phase precipitates are found within martensitic grains at 573 K. In contrast, radiation-induced precipitation is observed in the sample irradiated at the higher temperature.The formation of β-phase in Corrax irradiated at 773 K is evidenced by ChemiSTEM mapping and SAED analysis, as seen in Fig. 7(a and b), respectively. In

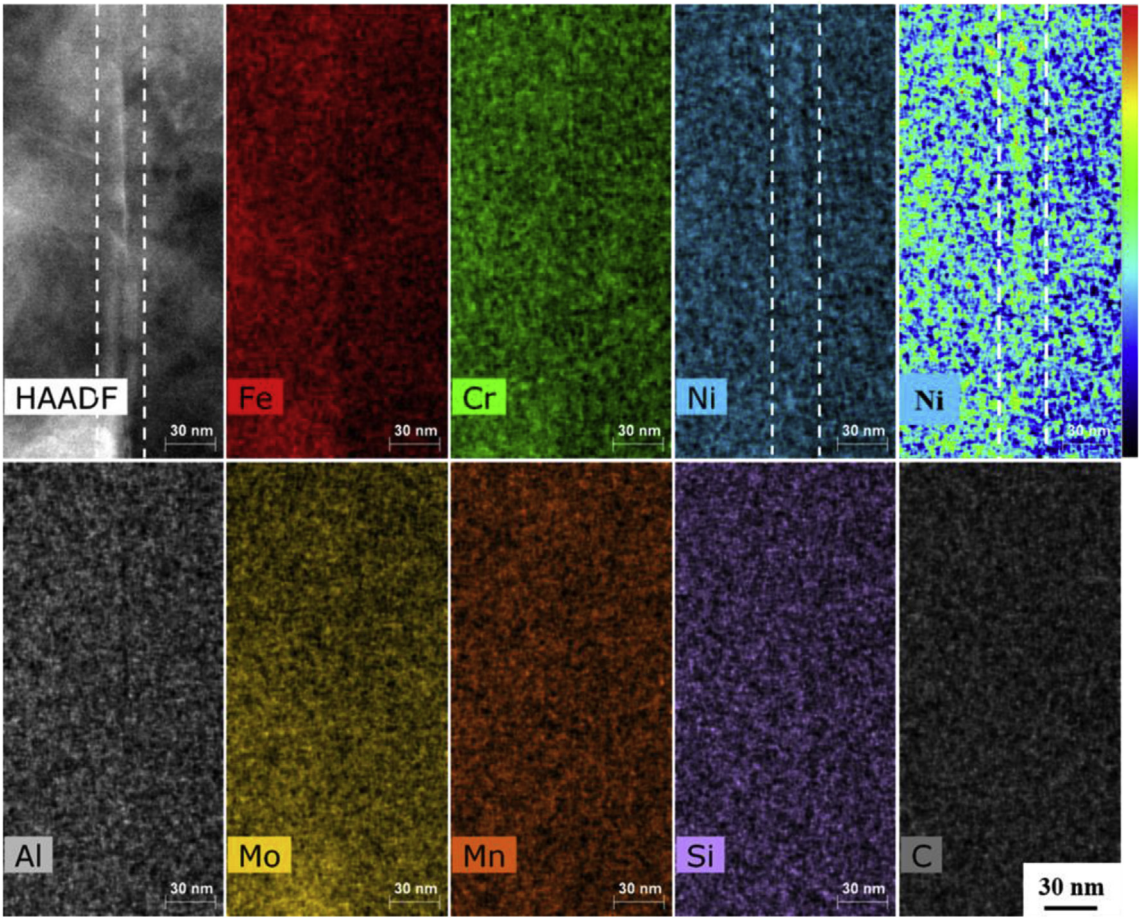

Fig. 6. Corrax ion irradiated to 10 dpa at 573 K: ChemiSTEM maps showing Ni segregates to the grain boundary.

addition, the (Cr, Mn, Mo)-rich Laves-phase precipitates with both spherical and elongated elliptical shapes are also observed in Corrax irradiated at 773 K, as evidenced in Fig. 8(a and b).

3.4. Precipitate size and number density measurements

Both β-phase and Laves-phase precipitates observed in Corrax irradiated at 773 K are similar to those observed in Corrax aged at 873 K, in terms of precipitate shape and chemical compositions. However, the precipitate size and number density are quite different. For the β-phase (see Fig. 9(a)), the average precipitate sizes are 5.0 nm and 11.9 nm and the number densities are 1.3×10^{23} m^{-3} and 1.8×10^{22} m^{-3} for the sample irradiated at 773 K and the sample thermally aged at 873 K, respectively. For the Laves-phase (see Fig. 9(b)), the average precipitate sizes are 10.5 nm and 15.9 nm and the number densities are 1.3×10^{22} m^{-3} and 4.0×10^{21} m^{-3} for the sample irradiated at 773 K and the sample thermally aged at 873 K, respectively. Overall, both the β-phase and Laves-phase observed in Corrax irradiated at 773 K have smaller average precipitate sizes and higher number densities compared with those observed in Corrax aged at 873 K, as indicated by a shift in the size distributions to larger precipitate size (Fig. 9(c and d)). Note that in terms of radiation resistance, a finer dispersion of higher number density is preferable.

3.5. Summary of observations

Both radiation and thermal aging induced precipitation and segregation in the PH 13-8 Mo maraging steel Corrax have been characterized. The comparisons among these results are summarized below:

- As for the thermal aging experiments, at the lower aging temperature (773 K), only early-stage precipitation occurs at grain boundaries whereas thermal aging-induced precipitation of β-phase and Laves-phase occurs significantly within martensitic grains at 873 K for an even shorter aging time (1 h vs. 3 h).
- As for the ion irradiation experiments, neither the β-phase nor the Laves-phase form under irradiation at 573 K up to 10 dpa whereas both precipitate population form under irradiation at 773 K. This suggest the existence of a threshold temperature for radiation enhanced precipitation to occur between 573 K and 773 K.
- As for the thermal aging and ion irradiation experiments performed at the same temperature (773 K) for a similar amount of experimental time (3 h), no precipitation occurs within martensitic grains in thermal aged Corrax whereas radiation-induced precipitation strongly occurs within martensitic grains in irradiated Corrax.

4. Discussion

4.1. Radiation-enhanced diffusion

The observations indicate radiation enhanced precipitation at 773 K due to two possible contributing factors, one on the nucleation aspect and one on the diffusional aspect. Indeed the higher number density of precipitates registered under irradiation may be

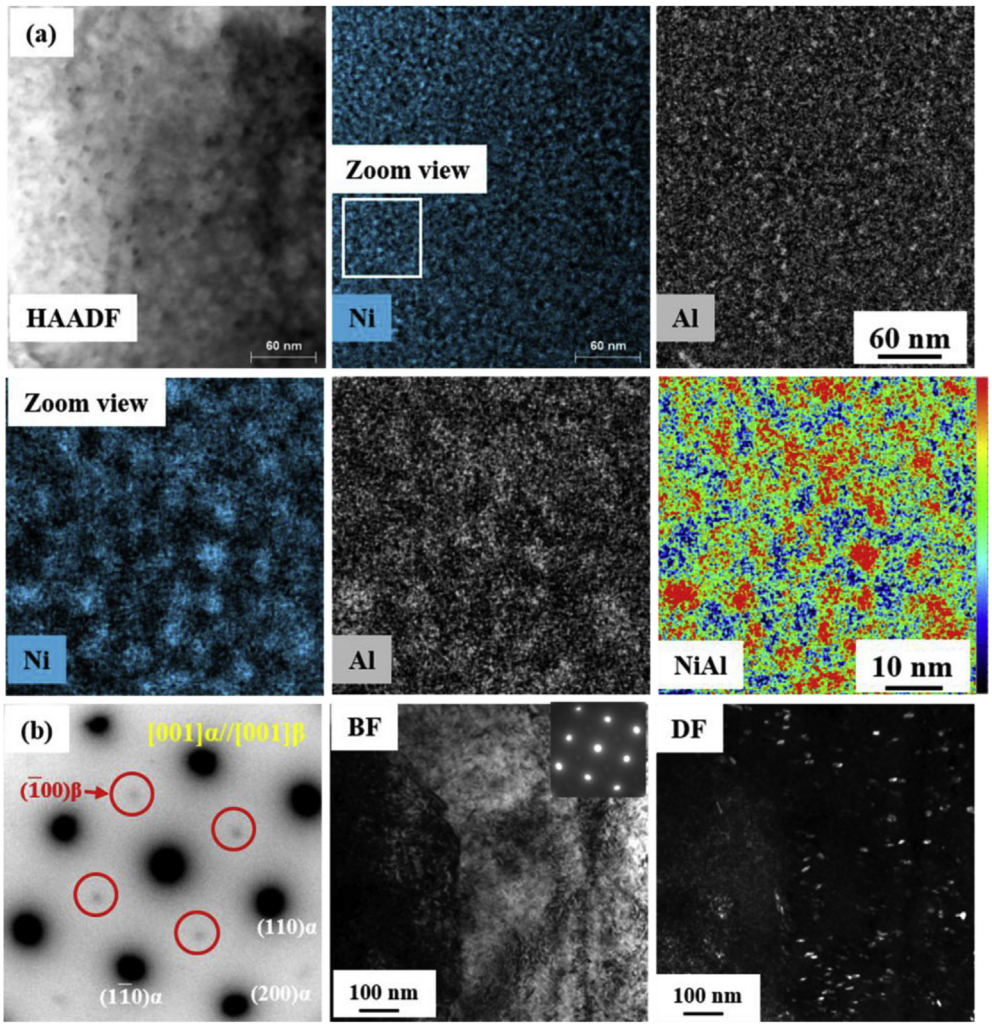

Fig. 7. Corrax ion irradiated to 5 dpa at 773 K: (a) ChemiSTEM maps showing the formation of (Ni,Al)-rich precipitates (a.k.a β-phase); (b) The SAED analysis showing the super-lattice reflections of β-phase and reflections of the martensitic matrix near the [100] zone axis. The precipitates are observed in the TEM-DF micrograph imaged with the $(\bar{1}00)$ super-lattice reflection.

due to an increased number of nucleation sites such as dislocations loops/segments since the irradiation produces such loops that can grow into a dislocation network. As shown in Table 3, the difference in dislocation density between thermal aging cases and irradiation cases is noticeable. Similar heterogeneous nucleation of (G-phase) precipitates and segregation of alloying elements at dislocations were experimentally observed in previous studies of ion irradiated Ferritic/Martensitic steels [30,31]. For those Ni and Si bearing alloys, cluster dynamics simulations indicated that both heterogeneous nucleation and radiation-induced segregation at dislocations are indeed necessary for the formation of G-phase [37]. Similarly, in this study, the higher density of dislocations in irradiated Corrax could provide more nucleation sites for the β-phase and Laves-phases.

The other contributing factor to the enhanced precipitation observed under irradiation is the enhanced diffusion due to the presence of large concentrations of point defects (vacancies and interstitials) generated by irradiation. In order to demonstrate the role of radiation-enhanced diffusion, diffusion coefficients under thermal aging and ion irradiation are estimated and compared with each other.

Only the analysis for the β-phase precipitation is described in detail below but the approach is similar for Laves-phase precipitation. Furthermore, in order to simplify the calculation and further model the precipitation, the multicomponent intermetallic β-phase is assumed as a single-component system, where the constituent with the slowest diffusivity in Fe controls the evolution kinetics. This simplification has been widely applied to studies of multi-component particles in Ni- and Fe-based alloys [38,39]. As seen in Table 2, the diffusion coefficients of Al in Fe at 773 K and 873 K are two orders of magnitude higher than those of Ni in Fe at the same temperatures [40,41]. Thus the diffusion coefficient of Ni can be considered to be the controlling factor for the kinetics of NiAl (β-phase) growth. Therefore, for D_{aging} at 773 and 873 K, we use the diffusion coefficients of Ni which are 3.54×10^{-21} and 4.14×10^{-19} $m^2\,s^{-1}$ at 773 and 873 K, respectively.

During irradiation, a large number of vacancies and interstitials are generated so that both the excess vacancies and interstitials may contribute to the radiation-enhanced diffusion. The enhanced diffusion coefficient (D_{irr}) is calculated using the approach which was applied to a similar problem as demonstrated in Hofer et al. [25]. D_{irr} is thus described as:

$$D_{irr} = D_v C_v + D_i C_i \tag{1}$$

where D_v and D_i are diffusion coefficients of vacancies and interstitials, and C_v and C_i are their concentrations.

The diffusion coefficients for vacancies D_v and D_i can be

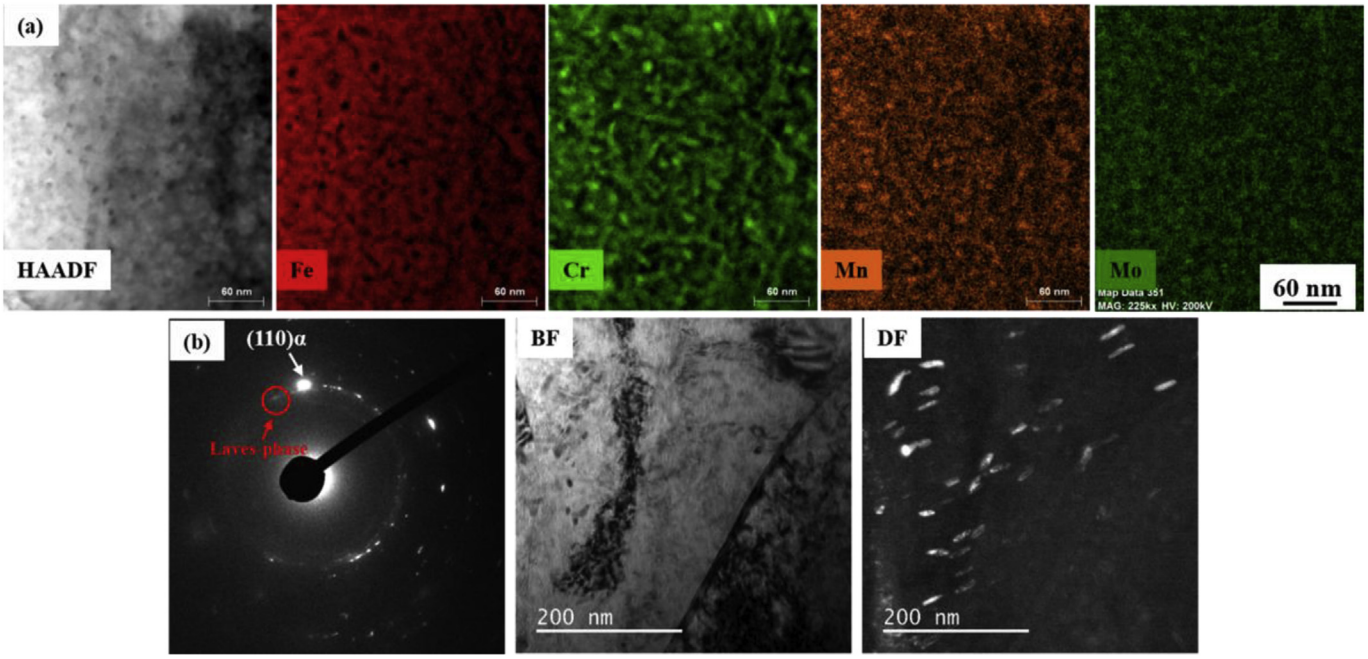

Fig. 8. Corrax ion irradiated to 5 dpa at 773 K: (a) ChemiSTEM maps showing the formation of (Cr,Mn,Mo)-rich precipitates (a.k.a Laves-phase); (b) TEM-BF and corresponding TEM-DF micrographs showing the formation of Laves-phase precipitates.

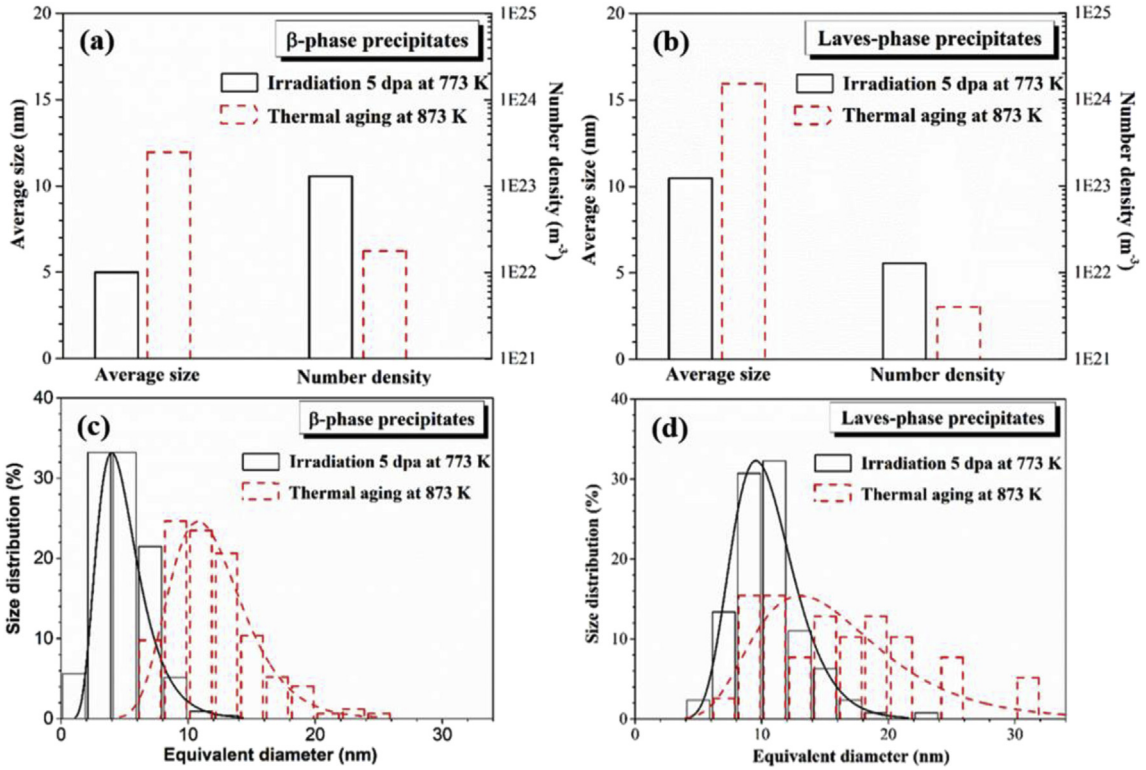

Fig. 9. (a–b) The average precipitate sizes and number densities of β-phase and Laves-phase in Corrax irradiated at 773 K and thermally aged at 873 K, respectively; (c–d) The precipitate size distributions of β-phase and Laves-phase, respectively. The bin size is set uniformly to 2 nm.

simplified using the well-known Einstein formula:

$$D_{x,\ x=v\ or\ i} = \frac{1}{6} * z(Aa_0)^2 \nu_D exp^{\left(\frac{-E_m^x}{kT}\right)} \quad (2)$$

where z is the number of nearest neighbors, Aa_0 is the jump distance which is related to the lattice parameter a_0 by the coefficient A. The values of z and A depend on the diffusion mechanism and the crystal structure. In the case of the vacancy mechanism of diffusion in a Body Centered Cubic (bcc) structure, $z = 8$ and $A = \frac{\sqrt{3}}{2}$.

Table 2
Summary of diffusivity values: The thermal diffusion coefficients are obtained from Refs. [34,35], and the radiation-enhanced diffusion coefficients are calculated using the equations described in section 4.1.

Thermal aging	at 773 K	at 873 K	Reference
D_{Ni} ($m^2 \cdot s^{-1}$)	3.54×10^{-21}	4.14×10^{-19}	[40]
D_{Al} ($m^2 \cdot s^{-1}$)	3.24×10^{-19}	2.96×10^{-17}	[41]
Ion irradiation	at 573 K	at 773 K	
D_v ($m^2 \cdot s^{-1}$)	8.78×10^{-12}	6.41×10^{-10}	Section 4.1
C_v	3.80×10^{-9}	1.19×10^{-10}	
D_i ($m^2 \cdot s^{-1}$)	2.58×10^{-10}	1.31×10^{-9}	
C_i	2.07×10^{-10}	9.28×10^{-11}	
D_{irr} ($m^2 \cdot s^{-1}$)	6.68×10^{-20}	1.52×10^{-19}	

Similarly, for the simple interstitial diffusion mechanism in a bcc structure, $z = 4$ and $A = \frac{1}{2}$. ν_D is the Debye frequency taken as $\approx 10^{13} s^{-1}$, and E_m^v and E_m^i are the vacancy migration energy and the interstitial migration energy, which are taken as ~0.63 eV [42,43] and ~0.31 eV [42,44], respectively. The vacancy and interstitial concentrations are then calculated based on the point defect balance equations derived from Rate Theory [45]. At steady state, the vacancy and interstitial concentrations (C_v^{ss} and C_i^{ss}) in the material are given by:

$$C_v^{ss} = -\frac{K_{is}C_s}{2*K_{iv}} + \left[\frac{K_0 K_{is}}{K_{iv}K_{vs}} + \frac{K_{is}^2 C_s^2}{4*K_{iv}^2}\right]^{\frac{1}{2}} \tag{3}$$

$$C_i^{ss} = -\frac{K_{vs}C_s}{2*K_{iv}} + \left[\frac{K_0 K_{vs}}{K_{iv}K_{is}} + \frac{K_{vs}^2 C_s^2}{4*K_{iv}^2}\right]^{\frac{1}{2}} \tag{4}$$

In the above equations, K_0 represents the defect production rate which can be obtained from the SRIM calculation. C_s represents the defect sink concentration. In our case, the most important sinks in irradiated Corrax are dislocations and therefore, the dislocation density ρ_d in Corrax irradiated at 573 and 773 K shown in Table 3 is included in the equation for the sink concentration:

$$C_s = \frac{\rho_d}{a_0} \tag{5}$$

The interstitials and vacancies are considered to migrate by random walk diffusion, being absorbed at unsaturable fixed sinks, or annihilating each other by mutual "recombination". In the proposed modeling effort, sinks and defects are assumed to be distributed homogeneously and no preferential absorption of specific point defects at specific sinks occurs. Thus, the vacancy-interstitial recombination rate K_{iv}, the interstitial-sink reaction rate coefficient K_{is} and the vacancy-sink reaction rate coefficient K_{vs} are as follows:

$$K_{iv} \approx 4*\pi*r_{iv}*D_i \tag{6}$$

$$K_{is} = 4*\pi*r_{is}*D_i \tag{7}$$

$$K_{vs} = 4*\pi*r_{vs}*D_v \tag{8}$$

where r_{iv}, r_{is} and r_{vs} are interaction radii for the reactions between the species. r_{is} and r_{vs} are approximately equal to the lattice parameter a_0, and r_{iv} is about twice as much [25,45].

Combining Eqs. (1)–(8), D_{irr} are calculated to be 6.68×10^{-20} and 1.52×10^{-19} $m^2 s^{-1}$ at 573 and 773 K, respectively.

Based on the above calculations, it is found that (i) the estimated D_{irr} at 773 K is two orders of magnitude higher than D_{aging} at the same temperature; (ii) the estimated D_{irr} at 773 K has the same order of magnitude as the thermal diffusion coefficient D_{aging} at 873 K. These calculation results are in agreement with the experimental results reported above, indicating that the precipitation observed in Corrax irradiated at 773 K is due to radiation-enhanced diffusion. It is to note that Hofer et al. [25] performed similar calculations but tracked the diffusion of Fe instead of Ni in the same material. The thermal diffusion coefficient D_{aging} at 773 K reported in Hofer et al. [25] is different from our calculation which is likely based on different input values due to the different element considered.

4.2. Modeling of precipitation kinetics

Classical precipitate nucleation and growth theories are used to estimate the nucleation rate and growth of the precipitates in our system. Theories are briefly reviewed with an emphasis on the three basic equations describing the nucleation, growth and coarsening processes. The nucleation rate of new precipitates is given by Ref. [46]:

$$J = N_0 Z \beta^* exp\left(-\frac{4\pi\gamma_p\left(r_p^*\right)^2}{3k_B T}\right) exp\left(-\frac{\tau}{t}\right) \tag{9}$$

where $N_0 = \frac{\rho_d}{a_0}$ is the number of nucleation sites (m^{-3}) for precipitation, $Z = \frac{V_m}{2\pi r_p^{*2}}\sqrt{\frac{\gamma_p}{k_B T}}$, $\beta^* = \frac{4\pi r_p^{*2} DX}{a_0^4}$ and $\tau = \frac{2}{\pi\beta^* Z^2}$ are constants dictated by the β-phase precipitate's molar volume V_m, critical radius for nucleation r_p^*, interfacial energy γ_p, the diffusion coefficient D, the matrix mean solute atom fraction X, the temperature T, the Boltzmann constant k_B and the lattice constant a_0.

The precipitate growth rate is given by Zener's law [39,47]:

$$\left.\frac{dr_p}{dt}\right|_{growth} = \frac{D(X - X^i)}{r_p(\alpha X^p - X^i)} \tag{10}$$

Table 3
Inputs used for modeling β-phase precipitation kinetics in thermal aged and irradiated Corrax.

	Parameter		Value	Reference
	Molar volume of NiAl V_m ($m^3 \cdot mol^{-1}$)		1.00×10^{-6}	[39]
	Interfacial energy of NiAl γ ($J \cdot m^{-2}$)		0.0204	
Thermal aging	Diffusion coefficients D_{aging} ($m^2 \cdot s^{-1}$)	at 773 K	3.54×10^{-21}	[40]
		at 873 K	4.14×10^{-19}	
	Dislocation density ρ_d (m^{-2})	at 773 K	2.40×10^{14}	Measured
		at 873 K	2.30×10^{14}	
Ion irradiation	Diffusion coefficients D_{irr} ($m^2 \cdot s^{-1}$)	at 573 K	6.68×10^{-20}	Table 2
		at 773 K	1.52×10^{-19}	
	Dislocation density ρ_d (m^{-2})	at 573 K	1.30×10^{15}	Measured
		at 773 K	1.12×10^{15}	

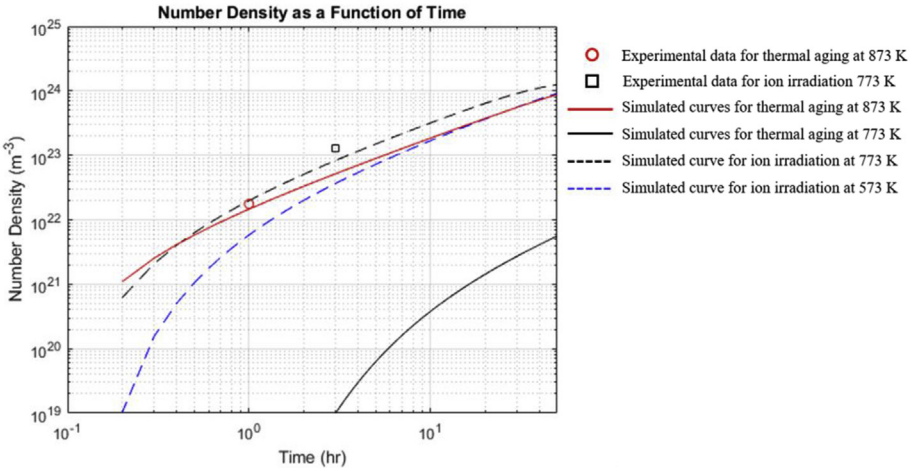

Fig. 10. Experimental and simulated precipitate number densities of β-phase as a function of time for thermal aging and ion irradiation at different temperatures.

where X^p and r_p are precipitate's molar composition and radius, respectively, X is the mean solute mole fraction in the matrix, and X^i is the equilibrium solute mole fraction at the matrix/precipitate interface which is given by the Gibbs-Thomson relation [48]:

$$X^i = K_{eq} exp\left(\frac{2\gamma_p V_m}{r_p R_g T}\right) \tag{11}$$

The critical radius dictates the minimum size to reach the critical energy for nucleation is then given as:

$$r_p^* = \frac{2\gamma_p V_m}{R_g T \ln\left(\frac{X}{K_{eq}}\right)} \tag{12}$$

where R_g is the gas constant and K_{eq} is a constant related to the mean solute mole fraction.

The precipitate coarsening rate is also given be the Gibbs-Thomson relation [46,48]:

$$\left.\frac{dr_p}{dt}\right|_{coarseining} = \frac{4R_0 DX^i}{27r_p^2(\alpha X^p - X^i)} \tag{13}$$

Eqs. (9)–(13) were encoded into the Matlab© where the parameters that define the number density were calculated at different times (t). The input parameters for the modeling are listed in Table 3. Plots of number density as a function of time were then able to be graphed. Fig. 10 shows the comparison between the experimental results and the modeling results, in terms of β-phase precipitate number density as a function of time.

- Comparing the aging and irradiation at 773 K, the simulation curve of irradiation is several orders of magnitude higher than that of aging. The simulation results support the assumption that diffusion is enhanced at 773 K due to irradiation so that the precipitation is accelerated at that temperature.
- For thermal aging at 873 K, the simulation curve is in good agreement with the experimental result. However, for the irradiation at 773 K, the simulation curve is lower than the experimental result.

The discrepancies between the experimental results and the simulation results may be attributed to several possible reasons.

- Firstly, the experimental number density could be over-estimated. Indeed, it is generally accepted that the thickness measured by EELS has an error of ~10%, as suggested by Malis et al. [32]. And the hand-counting process also contributes some error to the experimental results (by 10–15%).
- Secondly, dislocations are considered as primary nucleation sites for precipitation so that the nucleation rate is highly depends on the dislocation density. As a result, an under-estimation of dislocation density would also induce the simulated number density to be lower than the experimental one.
- Finally, the input values for the interstitial and vacancy migration energy are self-interstitials for Fe in pure α-Fe. We do recognize the fact that self-interstitials for Fe are likely different from segregation of alloying element Ni (and Al) in pure α-Fe. Therefore, the diffusion coefficient under ion irradiation could be under-estimated, inducing the simulated number density to be lower than the experimental one.

5. Conclusions

In this study, samples of Corrax were irradiated up to 10 dpa at 573 and 773 K using 1 MeV Kr ions, in-situ in the transmission electron microscope. The effects of irradiation were substantiated by comparing with the same material thermally aged at 773 and 873 K for similar amounts of experimental time.

The results indicate that both β-phase and Laves-phase precipitates form under irradiation in Corrax, with no aging treatments needed prior to irradiation. The precipitates formed under irradiation are characterized by a larger number density and finer size than under thermal aging. Using Rate Theory, it is demonstrated that radiation-enhanced diffusion can explain the formation and growth of the precipitates in the ion irradiated samples. Furthermore, a numerical model based on classical nucleation and growth theories for precipitation is introduced and shows a relatively good agreement with the experimental results in terms of precipitate density. This study serves to generate baseline data on ion irradiation effects on Corrax to learn how this steel responds to irradiation.

Acknowledgement

This work was supported by the U.S. Department of Energy, Office of Nuclear Energy under DOE Idaho Operations Office Contract DE-AC07-051D14517 as part of a Nuclear Science User Facilities experiment. The authors thank Pete Baldo, Ed Ryan, Jing Hu, Meimei Li and Mark Kirk at the IVEM facility for their assistance. Sample preparation and ChemiSTEM characterizations were

performed at the Analytical Instrumentation Facility (AIF) at North Carolina State University, which is supported by the State of North Carolina and the National Science Foundation (award number ECCS-1542015). The AIF is a member of the North Carolina Research Triangle Nanotechnology Network (RTNN), a site in the National Nanotechnology Coordinated Infrastructure (NNCI).

References

[1] S. Hossein Nedjad, S. Meimandi, A. Mahmoudi, T. Abedi, S. Yazdani, H. Shirazi, M. Nili Ahmadabadi, Effect of aging on the microstructure and tensile properties of Fe–Ni–Mn–Cr maraging alloys, Mater. Sci. Eng., A 501 (1) (2009) 182–187.
[2] G. Pantazopoulos, T. Papazoglou, P. Psyllaki, G. Sfantos, S. Antoniou, K. Papadimitriou, J. Sideris, Sliding wear behaviour of a liquid nitrocarburised precipitation-hardening (PH) stainless steel, Surf. Coating. Technol. 187 (1) (2004) 77–85.
[3] J.W. Morris Jr., Making steel strong and cheap, Nat. Mater. 16 (2017) 787.
[4] R.B. Frandsen, T. Christiansen, M.A.J. Somers, Simultaneous surface engineering and bulk hardening of precipitation hardening stainless steel, Surf. Coating. Technol. 200 (16) (2006) 5160–5169.
[5] J. Mittra, G.K. Dey, D. Sen, A.K. Patra, S. Mazumder, P.K. De, Solution quenched structure of wrought PH 13–8 Mo stainless steel, Scripta Mater. 51 (4) (2004) 349–353.
[6] H. Leitner, R. Schnitzer, M. Schober, S. Zinner, Precipitate modification in PH13-8 Mo type maraging steel, Acta Mater. 59 (12) (2011) 5012–5022.
[7] R. Schnitzer, M. Schober, S. Zinner, H. Leitner, Effect of Cu on the evolution of precipitation in an Fe–Cr–Ni–Al–Ti maraging steel, Acta Mater. 58 (10) (2010) 3733–3741.
[8] W. Sha, A. Cerezo, G.D.W. Smith, Phase chemistry and precipitation reactions in maraging steels: Part IV. Discussion and conclusions, Acta Mater. 24 (6) (1993) 1251–1256.
[9] S.-J. Kim, C.M. Wayman, Precipitation behavior and microstructural changes in maraging Fe-Ni-Mn-Ti alloys, Mater. Sci. Eng., A 128 (2) (1990) 217–230.
[10] V.K. Vasudevan, S.J. Kim, C.M. Wayman, Precipitation reactions and strengthening behavior in 18 Wt Pct nickel maraging steels, Metall. Trans. A 21 (10) (1990) 2655–2668.
[11] M. Schober, R. Schnitzer, H. Leitner, Precipitation evolution in a Ti-free and Ti-containing stainless maraging steel, Ultramicroscopy 109 (5) (2009) 553–562.
[12] A. Gemperle, J. Gemperlová, W. Sha, G.D.W. Smith, Aging behaviour of cobalt free chromium containing maraging steels, Mater. Sci. Technol. 8 (6) (1992) 546–554.
[13] R.D. Garwood, R.D. Jones, Electron microscope study of structure of a 25 percent Ni Ti Al maraging steel, Iron Steel INST J 204 (1966) 512.
[14] E.V. Pereloma, A. Shekhter, M.K. Miller, S.P. Ringer, Ageing behaviour of an Fe–20Ni–1.8Mn–1.6Ti–0.59Al (wt%) maraging alloy: clustering, precipitation and hardening, Acta Mater. 52 (19) (2004) 5589–5602.
[15] T.H. Simm, L. Sun, D.R. Galvin, P. Hill, M. Rawson, S. Birosca, E.P. Gilbert, H. Bhadeshia, K. Perkins, The effect of a two-stage heat-treatment on the microstructural and mechanical properties of a maraging steel, Materials 10 (12) (2017) 1346.
[16] V. Gray, D. Galvin, L. Sun, E.P. Gilbert, T. Martin, P. Hill, M. Rawson, K. Perkins, Precipitation in a novel maraging steel F1E: a study of austenitization and aging using small angle neutron scattering, Mater. Char. 129 (2017) 270–281.
[17] Z. Guo, W. Sha, D. Vaumousse, Microstructural evolution in a PH13-8 stainless steel after ageing, Acta Mater. 51 (1) (2003) 101–116.
[18] D.H. Ping, M. Ohnuma, Y. Hirakawa, Y. Kadoya, K. Hono, Microstructural evolution in 13Cr–8Ni–2.5Mo–2Al martensitic precipitation-hardened stainless steel, Mater. Sci. Eng., A 394 (1) (2005) 285–295.
[19] D.B. Miracle, Overview No. 104 the physical and mechanical properties of NiAl, Acta Mater. 41 (3) (1993) 649–684.
[20] P. Villars, L.D. Calvert, Pearson's Handbook of Crystallographic Data for Intermetallic Phases, American Society for Metals, Metals Park, OH, USA, 1985.
[21] M. Jong, F. Schmalz, J.W. Rensman, N.V. Luzginova, O. Wouters, J.B.J. Hegeman, J.G. van der Laan, Post-irradiation characterization of PH13-8Mo martensitic stainless steel, J. Nucl. Mater. 417 (1) (2011) 145–148.
[22] R.A. Gray, J.R. Hawthorne, Mechanical properties behavior of neutron irradiated 12Ni-5Cr-3Mo maraging steel plate and companion weld metal, Nucl. Eng. Des. 11 (3) (1970) 381–392.
[23] C.R. Cupp, E.P. Sadowski, L.P. Trudeau, Some effects of neutron irradiation on maraging steel, Trans. Metall. Soc. AIME 239 (9) (1967) 1468–1472.
[24] W. Van Renterghem, A. Al Mazouzi, S. Van den Berghe, Defect structure of irradiated PH13-8Mo steel, J. Nucl. Mater. 360 (2) (2007) 128–135.
[25] C. Hofer, E. Stergar, S.A. Maloy, Y.Q. Wang, P. Hosemann, An intermetallic forming steel under radiation for nuclear applications, J. Nucl. Mater. 458 (2015) 361–368.
[26] https://www.uddeholm.com/files/PB_Uddeholm_corrax_english.pdf.
[27] C. Zheng, S. Maloy, D. Kaoumi, Effect of dose on irradiation-induced loop density and Burgers vector in ion-irradiated ferritic/martensitic steel HT9, Philos. Mag. A 98 (2018) 2440–2456.
[28] J.F. Ziegler, M.D. Ziegler, J.P. Biersack, SRIM – the stopping and range of ions in matter, Nucl. Instrum. Methods Phys. Res. B 268 (11) (2010) 1818–1823, 2010.
[29] N. Juslin, K. Nordlund, J. Wallenius, L. Malerba, Simulation of threshold displacement energies in FeCr, Nucl. Instrum. Methods Phys. Res. B 255 (1) (2007) 75–77.
[30] C. Zheng, M.A. Auger, M.P. Moody, D. Kaoumi, Radiation induced segregation and precipitation behavior in self-ion irradiated Ferritic/Martensitic HT9 steel, J. Nucl. Mater. 491 (2017) 162–176.
[31] C. Zheng, D. Kaoumi, Radiation-induced swelling and radiation-induced segregation & precipitation in dual beam irradiated Ferritic/Martensitic HT9 steel, Mater. Char. 134 (2017) 152–162.
[32] T. Malis, S.C. Cheng, R.F. Egerton, EELS log-ratio technique for specimen-thickness measurement in the TEM, Microsc. Res. Tech. 8 (2) (1988) 193–200.
[33] Z. Huang, M.D. Abad, J.K. Ramsey, M.R. de Figueiredo, D. Kaoumi, N. Li, M. Asta, N. Gronbech-Jensen, P. Hosemann, A high temperature mechanical study on PH 13-8 Mo maraging steel, Mater. Sci. Eng., A 651 (2016) 574–582.
[34] S. Höring, D. Abou-Ras, N. Wanderka, H. Leitner, H. Clemens, J. Banhart, Characterization of reverted austenite during prolonged ageing of maraging steel CORRAX, Steel Res. Int. 80 (1) (2010) 84–88.
[35] G.S. Was, J.T. Busby, T. Allen, E.A. Kenik, A. Jensson, S.M. Bruemmer, J. Gan, A.D. Edwards, P.M. Scott, P.L. Andreson, Emulation of neutron irradiation effects with protons: validation of principle, J. Nucl. Mater. 300 (2) (2002) 198–216.
[36] J.I. Cole, T.R. Allen, G.S. Was, R.B. Dropek, E.A. Kenik, The influence of pre-irradiation heat treatments on thermal non-equilibrium and radiation-induced segregation behavior in model austenitic stainless steel alloys, in: M.L. Grossbeck, T.R. Allen, R.G. Lott, A.S. Kumar (Eds.), The Effects of Radiation Opt Materials. 21" International Symposium, ASTM STP 1447, ASTM International, West Conshohocken, PA, 2004.
[37] J.-H. Ke, H. Ke, G.R. Odette, D. Morgan, Cluster dynamics modeling of Mn-Ni-Si precipitates in ferritic-martensitic steel under irradiation, J. Nucl. Mater. 498 (2018) 83–88.
[38] M. Bonvalet, T. Philippe, X. Sauvage, D. Blavette, Modeling of precipitation kinetics in multicomponent systems: application to model superalloys, Acta Mater. 100 (2015) 169–177.
[39] E.I. Galindo-Nava, W.M. Rainforth, P.E.J. Rivera-Díaz-del-Castillo, Predicting microstructure and strength of maraging steels: elemental optimisation, Acta Mater. 117 (2016) 270–285.
[40] K. Hirano, M. Cohen, B.L. Averbach, Diffusion of nickel into iron, Acta Metall. 9 (5) (1961) 440–445.
[41] M. Salamon, H. Mehrer, Interdiffusion, Kirkendall effect, and Al self-diffusion in iron–aluminium alloys, Z. Metallkd 96 (1) (2005) 4–16.
[42] L. Malerba, M.C. Marinica, N. Anento, C. Björkas, H. Nguyen, C. Domain, F. Djurabekova, P. Olsson, K. Nordlund, A. Serra, D. Terentyev, F. Willaime, C.S. Becquart, Comparison of empirical interatomic potentials for iron applied to radiation damage studies, J. Nucl. Mater. 406 (1) (2010) 19–38.
[43] M.I. Mendelev, S. Han, D.J. Srolovitz, G.J. Ackland, D.Y. Sun, M. Asta, Development of new interatomic potentials appropriate for crystalline and liquid iron, Philos. Mag. A 83 (35) (2003) 3977–3994.
[44] F. Willaime, C.C. Fu, M.C. Marinica, J. Dalla Torre, Stability and mobility of self-interstitials and small interstitial clusters in α-iron: ab initio and empirical potential calculations, Nucl. Instrum. Methods Phys. Res. B 228 (1) (2005) 92–99.
[45] G.S. Was, Fundamentals of Radiation Materials Science, first ed., Springer, Verlag, Berlin, Heidelberg, 2007.
[46] M. Perez, M. Dumont, D. Acevedo-Reyes, Implementation of classical nucleation and growth theories for precipitation, Acta Mater. 56 (9) (2008) 2119–2132.
[47] M. Perrier, A. Deschamps, O. Bouaziz, Y. Brechet, F. Danoix, F. De Geuser, P. Donnadieu, K. Hoummada, P. Maugis, Characterization and modeling of precipitation kinetics in a Fe-Si-Ti alloy, Metall. Mater. Trans. 43 (13) (2012) 4999–5008.
[48] M. Perez, Gibbs–Thomson effects in phase transformations, Scripta Mater. 52 (8) (2005) 709–712.